In-Plane Direct-Write Assembly of Iridescent Colloidal Crystals

Alvin T. L. Tan, Sara Nagelberg, Elizabeth Chang-Davidson, Joel Tan, Joel K. W. Yang, Mathias Kolle, A. John Hart*

A. T. L. Tan
Department of Materials Science and Engineering
Massachusetts Institute of Technology
77 Massachusetts Ave, Cambridge, MA 02139, USA

S. Nagelberg, E. Chang-Davidson, Prof. M. Kolle, Prof. A. J. Hart
Department of Mechanical Engineering
Massachusetts Institute of Technology
77 Massachusetts Ave, Cambridge, MA 02139, USA
E-mail: ajhart@mit.edu

J. Tan, Prof. J. K. W. Yang
Pillar of Engineering Product Development
Singapore University of Technology and Design
8 Somapah Road, 487372, Singapore

Abstract

Materials made by directed self-assembly of colloids can exhibit a rich spectrum of optical

phenomena, including photonic bandgaps, coherent scattering, collective plasmonic

resonance, and wave guiding. The assembly of colloidal particles with spatial selectivity is

critical for studying these phenomena and for practical device fabrication. While there are

well-established techniques for patterning colloidal crystals, these often require multiple steps

including the fabrication of a physical template for masking, etching, stamping, or directing

de-wetting. Here, we present the direct-writing of colloidal suspensions as a technique for

fabrication of iridescent colloidal crystals in arbitrary two-dimensional patterns. Leveraging

the principles of convective assembly, the process can be optimized for high writing speeds

(~600 μm/s) at mild process temperature (30 °C) while maintaining long-range (cm-scale)

order in the colloidal crystals. The crystals exhibit structural color by grating diffraction, and

40 analysis of diffraction allows particle size, relative grain size and grain orientation to be

41 deduced. We present observations about the effect of write trajectory on particle ordering, and

42 provide insights for developing 3-D printing techniques for colloidal crystals via layer-wise

43 sintering.

44

45 **Main Text**

46 Nature is replete with instances of hierarchically structured materials that create visually

47 stunning appearances. For example, peacock feathers, butterfly wings, and beetle shells are

48 structured on the nano-, meso-, and macro-scales, resulting in iridescence and structural

49 color.[1–3] There is also much scientific interest and commercial value in creating similarly

50 structured man-made materials for applications including photonic devices and visual

51 displays.

52

53 These and other technology needs require materials fabrication techniques that provide

54 control of material structure over multiple length scales. Self-assembly provides a convenient

55 means for controlling material structure from the bottom up, and there has been substantial

56 research on convective self-assembly of colloidal particles into photonic crystals, including

57 seminal work by Vlasov[4] and others.[5–8] Patterned colloidal crystals have been created for

58 photonic devices and sensing applications.[9–11] However, these techniques often require the

59 prefabrication of templates or masks, and lithographic etching,[6,12] especially when spatial

60 control of the material is required. An alternate approach would be to print colloidal particles

61 directly onto the substrate from a digital template so that steps such as template fabrication,

62 masking, and etching, can be omitted. Printing from a digital template can be done with inkjet

63 printing, where droplets 20 to 50 µm in diameter are ejected on-demand from microscopic

64 nozzles.[13–16] However, the size of the droplet limits the grain sizes in the resulting colloidal

65 crystal, resulting in weak structural color.[17] Moreover, most inkjet printing techniques

66 require colloidal particle sizes to be limited from 50 to 300 nm for smooth printing,[16,18] and

67 printing larger particles presents nozzle clogging issues.

68

69 The combination of direct-write 3D printing with the principle of self-assembly is a potential

70 means to create new hierarchically-ordered materials. For instance, by dispensing a colloidal

71 solution onto a temperature-controlled substrate and coordinating the rate of crystal growth

72 with the retraction of the substrate, it is possible to fabricate colloidal crystals into specific

73 shapes, such as vertical pillars and helices.[19] Here, we extend this technique to the more

74 general case of planar direct-write self-assembly, where evaporation-induced assembly of

75 colloidal particles is guided by the moving meniscus traced by a motorized, liquid-dispensing

76 needle. We show that direct-write self-assembly can build high-quality iridescent colloidal

77 crystals in arbitrary patterns predetermined by a digital template.

78

79 Direct-write assembly is performed by the scheme shown in **Figure 1**a. A substrate, typically

80 a piece of silicon wafer or glass, is mounted onto a temperature-controlled (30 °C) precision

81 motion stage with a dispensing needle positioned slightly above the substrate. An aqueous

82 suspension of polystyrene particles (diameter $D = 746$ nm) is dispensed through the needle

83 and contacts the substrate, forming a liquid meniscus between the needle and the substrate.

84 Unlike slurry inks used in direct ink writing,[20,21] the concentration of the particles is low, and

85 therefore the flow properties of the suspension is similar to the solvent (i.e. water). The

86 substrate is then moved laterally by the stage, while maintaining the gap between the substrate

87 and the needle. As the substrate moves, particles are transported to the trailing edge of the

88 meniscus by an evaporation-induced flux. The particles are then compacted into a colloidal

89 crystal at the trailing edge of the meniscus. Therefore, a crystal can be written by relative

90 motion of the needle over the stage at a velocity matching the approximate rate of crystal

91 growth. An optical image of an exemplary colloidal crystal is shown in Figure 1c. By this

92   method, the trajectory of crystal growth can be influenced by multi-axial stage motion. As an

93   example, Figure 1b shows a serpentine-shaped crystal which appears iridescent to the naked

94   eye, made by coordinated in-plane motion of the stage beneath the needle.

95

96   For the purpose of studying the rate of crystal growth, we move the stage in a single direction

97   at a constant speed, denoted as the write speed. The layer thickness of the colloidal crystal can

98   be identified by its thin film interference colors.[22,23] In Figure 1c, blue regions correspond to

99   particle monolayers, green regions correspond to bilayers, and the brown regions correspond

100   to 3 or more layers of particles. We observe that the edge of the crystal is thicker than the

101   middle, a result of outward capillary flow towards the contact line of the meniscus. However,

102   the thickness of the middle region is uniform and can be controlled by the write speed, as will

103   be discussed in detail later. Scanning electron microscopy (SEM) imaging confirms the

104   presence of multiple layers of particles at the edge (Figure 1d) and a uniform crystal thickness

105   in the middle region. In the middle region, the particles are hexagonally packed, albeit with

106   typical crystal defects such as vacancies and dislocations.

107

108   The key to continuous direct-write self-assembly of colloidal crystals is matching the write

109   speed to the rate of crystal growth determined by evaporative flux from the trailing meniscus.

110   We can approximate the rate of crystal growth at the trailing end of the meniscus to be that of

111   other convective assembly techniques such as dip-coating and blade-casting. By considering

112   the balance of the rate of crystal growth with the flux of water and particles transported to the

113   crystal growth front, Dimitrov and Nagayama[24] proposed the following equation to calculate

114   the rate of crystal growth v_c:

$$v_c = \frac{\beta l j_e \varphi}{h(1-\varepsilon)(1-\varphi)} \qquad (1)$$

115   Here, h is the height of the crystal, ε its porosity, and φ is the volume fraction of particles in

116   suspension, as depicted in **Figure 2**a. Further, l is a characteristic evaporation length, j_e is the

117   water evaporation flux, and β is an interaction parameter between 0 and 1, where $\beta = 1$

118   corresponds to complete entrainment of particles by water flux. A particle monolayer is

119   denoted by $h = D$. By replacing the term $\beta l j_e$ with an experimentally fitted parameter K, as

120   previously demonstrated by Prevo and Velev,[25] we can create an operational phase diagram

121   which maps the relationship between experimental variables and crystallinity of the deposited

122   particles. From a series of experiments at different write speeds v and feedstock particle

123   concentrations φ, we identified disordered, ordered, and sub-monolayer phases, as plotted in

124   Figure 2b. The curve delineates the rate of crystal growth for a monolayer according to

125   Equation 1, with $\varepsilon = 0.605$ (corresponding to hexagonal close packing) and $K = 8 \times 10^4 \, \mathrm{m^2/s}$.

126   Below this line, ordered phases of at least single-particle thickness are obtained, such as

127   shown in Figure 2d. Above the line, the write speed v exceeds the rate of crystal growth v_c,

128   resulting in a sub-monolayer deposit, such as shown Figure 2e. Additionally, at very low

129   speeds, the particles are deposited as disordered aggregates, such as shown in Figure 2c.

130

131   This information serves as a practical guide for high throughput direct-write self-assembly. As

132   a case in point, the typical as-received concentration of commercial colloidal particles is $\varphi =$

133   0.025, which requires a write speed of ~50 μm/s for the crystalline phase. However, by

134   simply increasing the concentration of particles to $\varphi = 0.2$ via centrifugation and decanting,

135   the concentrated particle suspension can then be used to boost write speed by an order of

136   magnitude to ~600 μm/s.

137

138   By motorized stage motion, a colloidal crystal can be directly patterned using a digital

139   template (e.g., starting with a vector graphic, Figure S1), without the need for further process

140 steps such as etching. The colloid suspension is dispensed at a constant rate while translating

141 the stage according to the script, resulting in a patterned colloidal crystal in the shape of the

142 vector graphic, as shown in **Figure 3**.

143

144 The general iridescence visible throughout the colloidal crystal indicates a high degree of

145 crystallinity. Conversely, the small regions that lack iridescence indicate lack of particle

146 order. Specifically, these regions occur where there was a turn or overlap in the toolpath,

147 suggesting that the toolpath trajectory can have a strong influence on self-assembly.

148 Moreover, the local curvature of the toolpath affects order, and the limiting cases are revealed

149 in Figure 3 i, iii and iv. In the limit of a straight line (Figure 3 iii) or wide arc (Figure 3 i),

150 crystallinity is maintained. In contrast, in the limit of a sharp 90 ° turn, a white patch appears

151 on the inside of the turn which indicates a region of disorder. Thus, the appearance of

152 iridescence provides visual feedback on the degree of order or disorder of the colloidal

153 assembly.

154

155 Next, we performed a series of experiments with different tool path curvatures. We denote the

156 inner radius of curvature as R and the width of the colloidal trail as W (Figure 3c).

157 Micrographs shown in Figure 3c-f depict colloidal trails with progressively smaller R, yet

158 constant W (governed by the needle diameter). In general, as R decreases relative to W, the

159 deposit of particles on the inside of the turn becomes thicker and eventually becomes

160 disordered when $R < W$. This observation is in general agreement with the phase diagram

161 (Figure 2b), which shows that slow write speeds lead to disordered deposits. The deposition

162 rate of particles relative to the local tangential velocity is inversely proportional to the local

163 curvature of the path. In the experimental conditions for Figure 3f, the volume fraction of

164 particles is $\varphi = 0.05$ and the tangential velocity at the middle of the tool path is $v_1 = 146$ μm/s.

165 The radius of curvature at the middle of the toolpath is $R_1 = 500$ μm and the inside radius of

166 curvature of the toolpath is $R_2 = 140$ μm. Therefore, the tangential velocity at the inside of the

167 toolpath is $v_2 = (R_2/R_1)v_1 = 40$ μm/s. These conditions ($\varphi = 0.05$, $v_2 = 40$ μm/s) corresponds to

168 the onset of disorder in Figure 2b.

169

170 The direct-write colloidal crystals exhibit structural colors that depend on the local crystalline

171 order, lighting, and viewing conditions. The primary mechanisms by which structural colors

172 are commonly created are broadly categorized into thin film interference, multilayer

173 interference, grating diffraction, and other interference phenomena; each is enabled by nano-

174 to micro- scale periodicity on the order of the wavelength of visible light.[26]

175

176 To characterize the light scattering and iridescence of a printed colloidal crystal, we

177 illuminated the sample with collimated light such that the reflected light was projected onto

178 the inside of a ping-pong ball, as illustrated in Figure 5c. This technique allows colors from

179 all viewing angles to be visualized in a single image.[27] A sample with small grains (prepared

180 at $v = 610$ μm/s with $\varphi = 0.10$) is shown in **Figure 4**a, and the corresponding color projection

181 is displayed in Figure 4d. The separation of color leads us to hypothesize that the colloidal

182 crystal acts as a reflective diffraction grating, because shorter wavelengths are diffracted at

183 smaller angles with respect to the normal, as one would expect from the grating equation

$$m\lambda = d(\sin\theta_i + \sin\theta_r) \tag{2}$$

184 Where m is the diffraction order, d is the grating spacing, θ_i and θ_r are respectively the angles

185 of incident and diffracted rays relative to the normal. In our experimental conditions, m = 1

186 since we observe only one diffraction order, $\theta_i = 0°$ since the incident ray is normal to the

187 sample, and $d = \sqrt{3}/2D$ since the particles are arranged in a hexagonal lattice with center-to-

188 center distance of D.

189

190   The colors on the hemispherical screen in Figure 4d can be linearly mapped with respect to

191   polar angle θ and azimuthal angle ϕ, yielding Figure 4e. From Figure 4e, the radiant intensity

192   can be averaged over all values of ϕ and plotted as a function of θ for each of the camera's

193   three color channels, as shown in Figure 4f. The peaks can be used, in conjunction with

194   Equation 2, to estimate particle size by using λ = 490, 550, and 650 nm as the peak

195   wavelengths for the blue, green, and red channels respectively.[28] This yielded an estimated

196   particle diameter of 751 nm, which matches the known colloid diameter of 746 ± 22 nm.

197

198   If there are many small colloidal crystal grains with different orientations present (such as for

199   the sample shown in Figure 4a), each diffracting light toward a different azimuthal angle (ϕ),

200   the scattered radiant intensity is almost constant along all azimuthal angles. However, if there

201   are only a few grains present, distinct peaks are visible in the color projections. When the

202   same experiment is performed with a large-grain sample (Figure 4b, prepared at v = 30 μm/s

203   with φ = 0.025), distinct diffraction peaks are observed, as shown in Figure 4g and 4h. The

204   six-fold symmetry of the diffraction pattern projected onto the sphere indicates that the

205   particles assume a hexagonal arrangement.

206

207   Moreover, by analyzing the relative intensities of the peaks, it is possible to deduce

208   information about the size proportions of the grains present in the illuminated region. To

209   perform this analysis, we extracted the radiant intensity as a function of the azimuthal angle ϕ

210   at a polar angle θ = 52° (see area marked in Figure 4h) and plotted the data as Figure 4i. Due

211   to the six-fold symmetry of the diffraction pattern, the data is collapsed onto ϕ = 0 to ϕ = 60°.

212   The highest and second-highest peaks should correspond to the largest and second-largest

213   grains, which we designate as grains A and B, respectively. The radiant intensity level marked

214   by the black solid line should then correspond to the much smaller grains of various

215   orientations, which we designate as C. By comparing the relative peak intensities, we

216   calculate that the area fraction of the various grain structures are $f_A = 0.41 \pm 0.14$, $f_B = 0.11 \pm$

217   0.06, and $f_C = 0.48 \pm 0.17$ (see SI for description of calculation). This result may be compared

218   to the direct measurement of relative grain sizes via image analysis. An optical micrograph of

219   the illuminated region is shown in Figure 4j, with the A, B, and C structures identified and

220   labelled. By image segmentation, we measured $f_A = 0.32$, $f_B = 0.09$, and $f_C = 0.59$. Given the

221   large uncertainty in the peak signal for A, the estimates from the diffraction peak intensities

222   are in reasonable agreement with the measurements from the micrograph. Finally, using SEM

223   (Figure 4k), we measured that grains A and B are misoriented by 19.5°. This is in close

224   agreement with the radiant intensity plot (Figure 4i), which shows the A and B peaks 20°

225   apart.

226   Sequential deposition of particles in multiple write passes, such as in overlapping or

227   intersecting patterns, could facilitate the use of colloidal assembly for 3-D printing. However,

228   we initially found that an overlap in the direct-write toolpath results in disorder, as shown in

229   Figure 3b-ii. We hypothesize that this is due to the array of particles from the first pass being

230   broken up by the liquid meniscus during the second pass. Therefore, if the particles from the

231   first pass are effectively immobilized, then it may be possible to preserve crystallinity for

232   multiple passes to build up 3-D prints.

233

234   One means of immobilizing the particle array is to sinter the particles. To sinter the particles,

235   a colloidal crystal sample was heated to 110 °C for 15 minutes, followed by 1 minute of

236   oxygen plasma treatment. The oxygen plasma improves the wettability of the surface, which

237   becomes hydrophobic after the heating step. The sintering causes a slight color change in the

238   colloidal crystal due to necks forming between the particles, which reduces the interparticle

239   spacing. A second pass of direct-writing was then performed atop the first pass, as shown in

240   Figure 3h. Separately, a second pass of direct-writing was also performed on a control sample

241   which was not sintered, as shown in Figure 3g. The preservation of structural color on the

242   sintered sample, compared to the whitish regions on the control sample, shows that sintering

243   was effective in immobilizing the particle array from the first pass, allowing the particles on

244   the second pass to self-assemble on the sintered array with crystalline registry. SEM confirms

245   particle order on the second pass for the sintered sample (Figure 3i), and particle disorder on

246   the second pass for the control sample (SI Figure S2). Potentially, layer-by-layer sintering

247   (e.g., by in situ infrared heating) of the particles could be employed for building up multilayer

248   structures with crystalline registry of the particles, which would be a means of 3-D printing

249   colloidal crystals.

250

251   Additionally, we explore how the direct-write technique could be employed to assemble

252   diverse colloidal assemblies with the potential for more functionality. As a simple example, in

253   **Figure 5**, we demonstrate direct-writing of colloidal crystals comprising of different particle

254   sizes (500 nm, 746 nm, and 1 µm) and different particle compositions (PS, PMMA, and

255   silica) on the same silicon wafer. Figure 5 also demonstrates the limits to the width of the

256   crystal that can controlled by the diameter of the needle. Although smaller needles may be

257   used for direct-write assembly, the width of the crystal is not strictly proportional to the

258   diameter of the needle, as shown from the progression of needle sizes from 22 gauge (OD, ID

259   = 0.7, 0.4 mm) to 27 gauge (OD, ID = 0.4, 0.2 mm) to 33 gauge (OD, ID = 0.2, 0.1 mm).

260   With the smallest needle size, 33 gauge, the crystal width was similar to that of the 27 gauge

261   due to spontaneous spreading of the liquid meniscus that is difficult to control even at very

262   low dispense rates (1.57 nL/s), as shown in SI Figure S3. Yet, spreading of the liquid

263   meniscus at a finite contact angle is necessary for successful deposition of particles.[29,30]

264   Future work on direct-writing of colloids could include exploring the technique's ultimate

265   resolution limits by tuning the hydrophilicity of the surface via plasma treatment or pre-

266 depositing molecular self-assembled monolayers onto the substrate to control spreading of the

267 meniscus.

268

269 In conclusion, we demonstrated freeform fabrication of colloidal crystals by in-plane direct-

270 write self-assembly, and experimentally derived an operational phase diagram, which maps

271 write speeds and particle concentrations that lead to crystalline features. Furthermore, we

272 investigated the effect of toolpath trajectory on the crystallinity of the colloidal assemblies,

273 and showed that sintering can be used to stack overlapping passes. We also established

274 grating diffraction as the mechanism for the structural color effects in these colloidal crystals,

275 and showed that simple characterization of the optical properties of the crystals yields reliable

276 information about microstructure, such as particle size, grain size, and orientation. In future

277 work, in-plane direct-write assembly could be extended to a practical technique for 3-D

278 printing of colloidal crystals if a means for rapidly sintering each layer could be developed.

279 Finally, we note that, while macroscopic printed features can be well-controlled by the direct-

280 write toolpath, at the microstructural level, every trace or image that is printed with direct-

281 write is unique, which suggests applications of direct-write in generating patterns for use in

282 optical encoding and security devices.

283
284
285 **Experimental Section**

286 *Direct-write self-assembly*: An aqueous suspension of polystyrene particles (750 nm diameter,

287 Polysciences Inc.) was loaded into a 100 µl syringe (Hamilton 1710 RN) affixed with a blunt

288 tip needle (Hamilton point style 3, 27ga) and placed into a custom-made holder. The plunger

289 of the syringe is depressed using a linear actuator (M-229.26S, Physik Instrumente)

290 commanded from a computer. The stage is heated to 30±0.1 °C by a thermoelectric chip

291 (Custom Thermoelectric) and the stage temperature is measured by an embedded K-type

292 thermocouple (Omega) fed to a temperature controller (PTC 10, Stanford Research Systems).

293 The stage is actuated by linear motors (Zaber LRM025A- E03T3-MC03) controlled by a

294 two-axis stepper motor controller (Zaber X-MCB2- KX14B) via the Zaber Console software.

295 To perform direct-write in complex trajectories, the shapes were drawn using Carbide Create

296 software, and the G-code was converted into native motor commands using the G-code

297 translator in the Zaber Console software.

298 *Microstructural characterization*: Optical images were taken using a Zeiss Smartzoom optical

299 microscope. Images were taken in coaxial lighting mode (Fig. 1c, 2c, 2d, 2e, 5j) to clearly

300 distinguish monolayers, bilayers, and multilayers. Images were taken in ring lighting mode

301 (Fig. 3, 4, 5a, 5b) to clearly distinguish iridescent and non-iridescent regions. SEM was

302 performed with a Zeiss Merlin High Resolution SEM in high efficiency secondary electron

303 imaging mode, at an accelerating voltage of 1 kV and probe current of 100 pA. Image

304 analysis was performed using ImageJ.

305 *Characterization of optical properties*: The colloidal crystal sample was illuminated by a light

306 source (Ocean Optics HL-2000) directed by an optical fiber (Thorlabs M25L01, ø200μm,

307 0.22 NA) to a collimating lens (Thorlabs F230SMA-A, alignment wavelength = 543 nm, f =

308 4.34 mm, NA = 0.57). The collimated light was directed to shine through a hole drilled

309 through a translucent hemispherical screen (half a ping pong ball) and onto the sample placed

310 in the middle of the enclosing hemisphere. The light projected onto the screen was recorded

311 with a DSLR camera (Canon EOS Rebel T3i) which was fixed in position using an articulated

312 arm.

313 **Supporting Information**
314 Supporting Information is available from the Wiley Online Library or from the author.
315
316

321 and by the MIT-Skoltech Next Generation Program. A.T.L.T. was supported by a
322 postgraduate fellowship from the Singapore Defence Science Organization. S.N. and M.K.
323 were supported by the US Army Research Office through the Institute for Soldier
324 Nanotechnologies at MIT, under contract number W911NF-13-D-0001 and by the National
325 Science Foundation's CBET programme on "Particulate and Multiphase Processes" under
326 grant numbers 1804241 and 1804092. E.C.D. was supported by the MIT Undergraduate
327 Research Opportunities Program (UROP). J.T. was supported an SUTD international UROP
328 award. J.K.W.Y. acknowledges funding from National Research Foundation Competitive
329 Research Programme Grant No. CRP20-2017-0004. This work made use of the MRSEC
330 Shared Experimental Facilities at MIT, supported by the National Science Foundation under
331 award number DMR-14-19807.
332
333   Received: ((will be filled in by the editorial staff))
334   Revised: ((will be filled in by the editorial staff))
335 Published online: ((will be filled in by the editorial staff))
336

337 **References**

338 [1] S. Kinoshita, S. Yoshioka, *ChemPhysChem* **2005**, *6*, 1443.
339 [2] M. Kolle, U. Steiner, in *Encycl. Nanotechnol.*, Springer Netherlands, Dordrecht, **2019**,
340   pp. 3840–3854.
341 [3] S. L. Burg, A. J. Parnell, *J. Phys. Condens. Matter* **2018**, *30*, 413001.
342 [4] Y. A. Vlasov, X. Z. Bo, J. C. Sturm, D. J. Norris, *Nature* **2001**, *414*, 289.
343 [5] N. D. Denkov, O. D. Velev, P. A. Kralchevsky, I. B. Ivanov, H. Yoshimura, K.
344   Nagayama, *Nature* **1993**, *361*, 26.
345 [6] A. Van Blaaderen, R. Ruel, P. Wiltzius, *Nature* **1997**, *385*, 321.
346 [7] P. Jiang, J. F. Bertone, K. S. Hwang, V. L. Colvin, *Chem. Mater.* **1999**, *11*, 2132.
347 [8] Y. Xia, B. Gates, Y. Yin, Y. Lu, *Adv. Mater.* **2000**, *12*, 693.
348 [9] Y. Cui, M. T. Björk, J. A. Liddle, C. Sönnichsen, B. Boussert, A. P. Alivisatos, *Nano
349   Lett.* **2004**, *4*, 1093.
350 [10] I. B. Burgess, L. Mishchenko, B. D. Hatton, M. Kolle, M. Lončar, J. Aizenberg, *J. Am.
351   Chem. Soc.* **2011**, *133*, 12430.
352 [11] J. Hou, M. Li, Y. Song, *Angew. Chemie Int. Ed.* **2018**, *57*, 2544.
353 [12] Y. Yin, Y. Lu, B. Gates, Y. Xia, *J. Am. Chem. Soc.* **2001**, *123*, 8718.
354 [13] J. Park, J. Moon, H. Shin, D. Wang, M. Park, *J. Colloid Interface Sci.* **2006**, *298*, 713.
355 [14] J. Park, J. Moon, *Langmuir* **2006**, *22*, 3506.
356 [15] L. Wang, J. Wang, Y. Huang, M. Liu, M. Kuang, Y. Li, L. Jiang, Y. Song, *J. Mater.
357   Chem.* **2012**, *22*, 21405.
358 [16] L. Cui, Y. Li, J. Wang, E. Tian, X. Zhang, Y. Zhang, Y. Song, L. Jiang, *J. Mater.
359   Chem.* **2009**, *19*, 5499.
360 [17] H. Nam, K. Song, D. Ha, T. Kim, *Sci. Rep.* **2016**, *6*, 30885.
361 [18] J. Wang, L. Wang, Y. Song, L. Jiang, *J. Mater. Chem. C* **2013**, *1*, 6048.
362 [19] A. T. L. Tan, J. Beroz, M. Kolle, A. J. Hart, *Adv. Mater.* **2018**, *30*, 1803620.
363 [20] J. E. Smay, J. Cesarano, J. A. Lewis, *Langmuir* **2002**, *18*, 5429.
364 [21] J. A. Lewis, *Adv. Funct. Mater.* **2006**, *16*, 2193.
365 [22] M. Bedewy, J. Hu, A. J. Hart, in *2017 IEEE 17th Int. Conf. Nanotechnology, NANO
366   2017*, IEEE, **2017**, pp. 286–289.
367 [23] H. Cong, W. Cao, *Langmuir* **2004**, *20*, 8049.
368 [24] A. S. Dimitrov, K. Nagayama, *Langmuir* **1996**, *12*, 1303.
369 [25] B. G. Prevo, D. M. Kuncicky, O. D. Velev, *Colloids Surfaces A Physicochem. Eng.*

370   *Asp.* **2007**, *311*, 2.

371   [26]   S. Kinoshita, S. Yoshioka, J. Miyazaki, *Reports Prog. Phys.* **2008**, *71*, 076401.

372   [27]   A. E. Goodling, S. Nagelberg, B. Kaehr, C. H. Meredith, S. I. Cheon, A. P. Saunders,

373   M. Kolle, L. D. Zarzar, *Nature* **2019**, *566*, 523.

374   [28]   J. Deglint, F. Kazemzadeh, D. Cho, D. A. Clausi, A. Wong, *Sci. Rep.* **2016**, *6*, DOI

375   10.1038/srep28665.

376   [29]   R. D. Deegan, O. Bakajin, T. F. Dupont, G. Huber, S. R. Nagel, T. a Witten, *Nature*

377   **1997**, *389*, 827.

378   [30]   R. Deegan, *Phys. Rev. E* **2000**, *61*, 475.

379

380

381
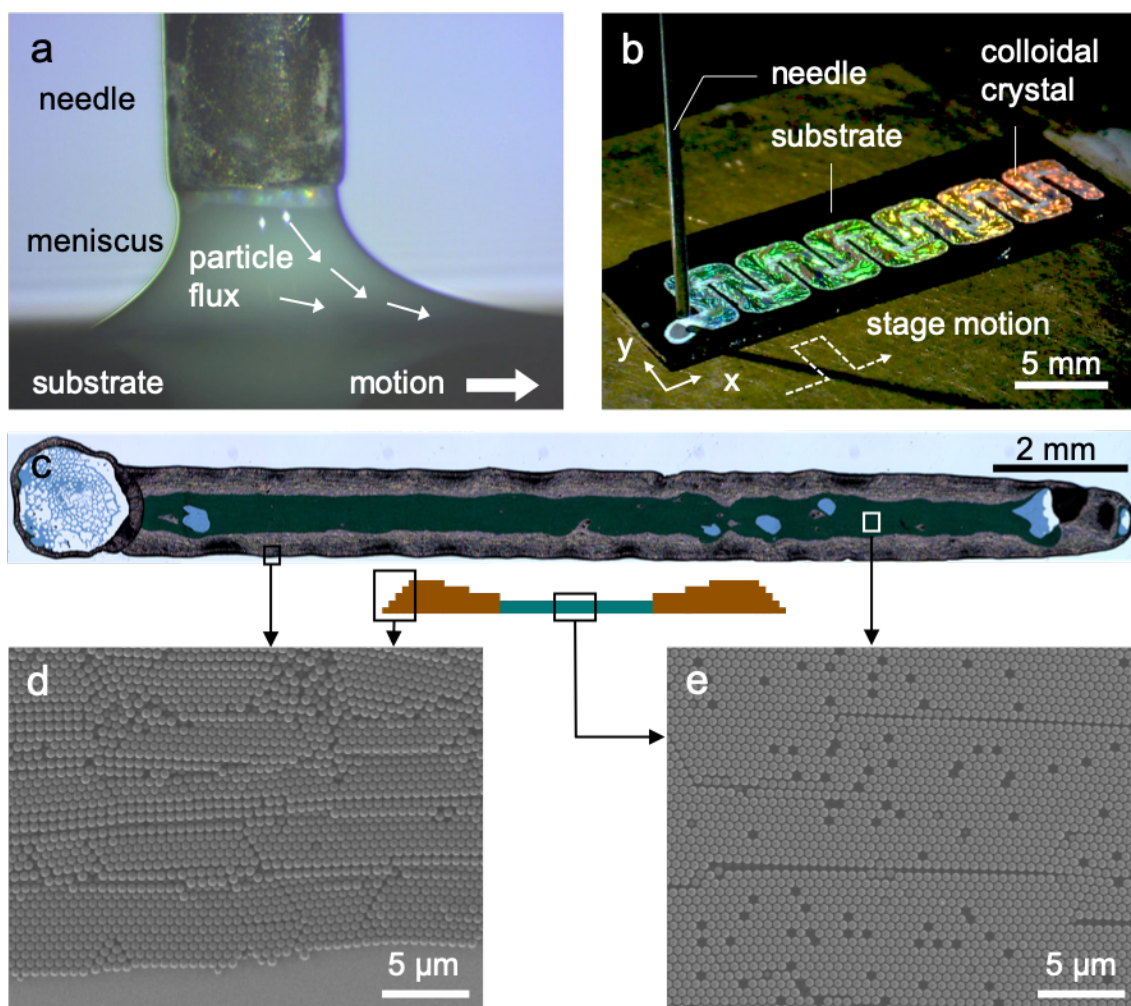
382
383
384 **Figure 1.** Fabrication of colloidal crystals by in-plane direct-write self-assembly. (a) In-plane
385 direct-write self-assembly is performed by precision dispense of a colloidal suspension from a
386 needle, coupled with lateral substrate motion. (b) A serpentine colloidal crystal is drawn by
387 movement of the stage. (c) Optical image (top) and cross-section schematic (bottom) of an
388 exemplary colloidal crystal trace. The edge of the crystal (brown coloration) is thicker than
389 the middle. The middle consists of mostly particle bilayers (green coloration) and monolayers
390 (blue coloration). (d) SEM image showing multilayer terraces at the edge of the crystal. (e)
391 SEM image of the middle region of the crystal showing defects such as dislocations and
392 vacancies.
393
394
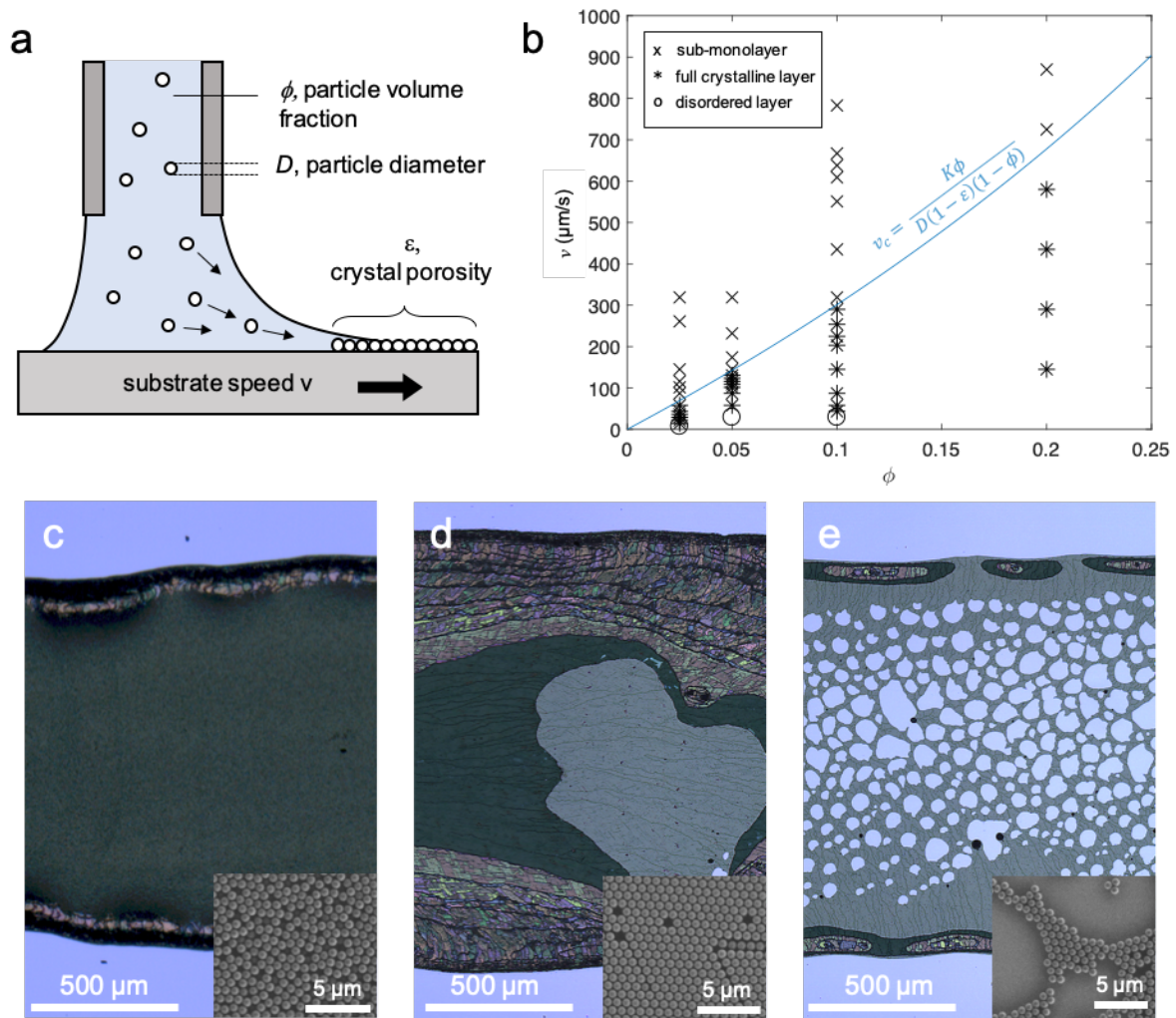
Figure 2. Optimization of direct-write process parameters to achieve well-packed crystalline deposits. (a) Schematic of the direct-write assembly process, where ϕ is the volume fraction of particles in solution, D is the particle diameter, ε is the porosity of the colloidal crystal, and v is the substrate speed. (b) An operational phase diagram where disordered, ordered, and sub-monolayer phases are plotted as a function of ϕ and v. The curve delineates the natural assembly speed as modelled by the Dimitrov-Nagayama equation with fitting parameter K. (c-e) Optical microscope images and inset SEM of colloid trails with (c) disordered, (d) ordered, and (e) sub-monolayer phases.
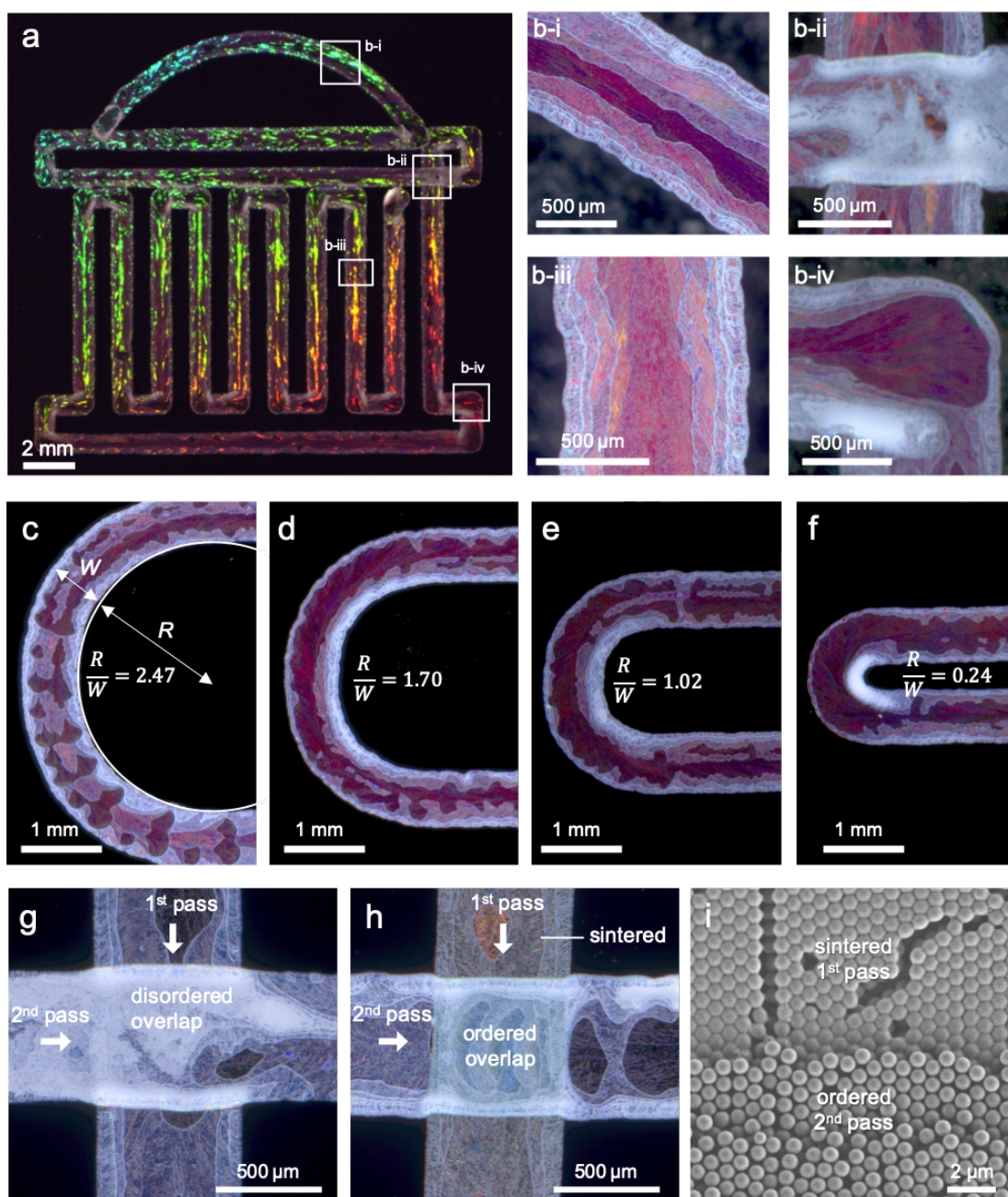
Figure 3. Effect of direct-write tool path on crystal order. (a) Photograph of a colloidal crystal patterned by control of the direct-write trajectory. (b) Optical microscope enlargements showing the morphology of a (b-i) wide arc, (b-ii) overlap, (b-iii) straight line, and (b-iv) sharp turn. (c-f) The crystallinity of a colloidal trail is affected by curvature of the direct-write trajectory, as demonstrated by trails with turning radius (R) of (c) 1.63 mm, (d) 1.12 mm, (e) 0.67 mm, and (f) 0.16 mm, and constant width $W = 0.66$ mm. Generally, the inside of the curved trail is ordered when $R/W > 1$ but becomes disordered when $R/W < 1$. (g-h) Optical images of perpendicular overlapping trails. (g) Without sintering, overlapping colloidal trails result in disorder, as apparent from the whitish region on the trail from the second pass. (h) After sintering of the trail from the first pass, the trail from the second pass is deposited atop with crystalline arrangement. (i) SEM image of a sintered first pass and an ordered second pass.
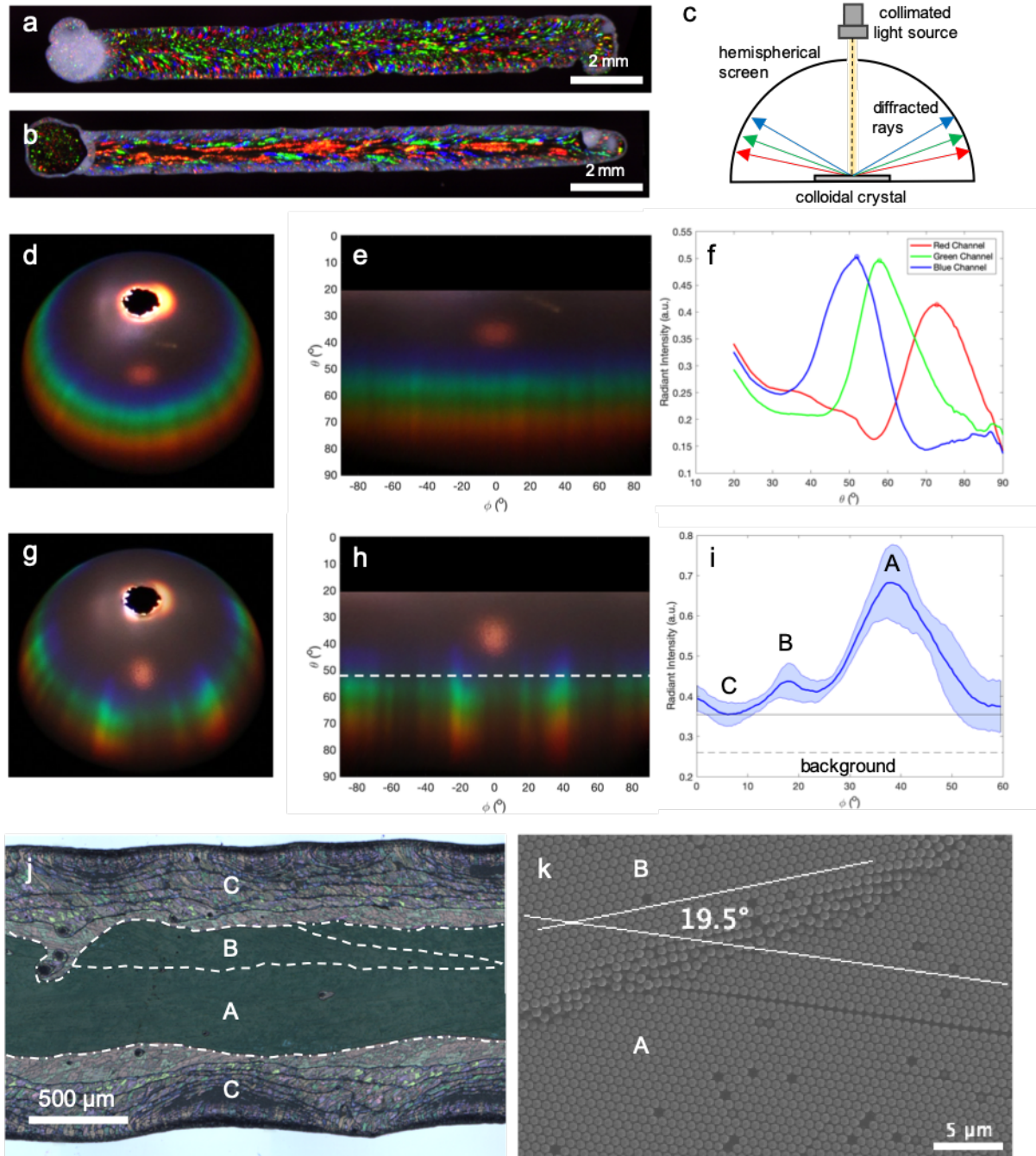
Figure 4. Optical properties of direct-write colloidal crystals. (a,b) Photographs of (a) small-grain and (b) large-grain colloidal crystal imaged under ring lighting around the objective lens. (c) Schematic depicting the characterization of optical properties by illuminating the colloidal crystal with collimated light at an angle normal to the crystal and observing the projection of diffracted colors on a hemispherical screen. (d,g) Photograph of colors projected from the (d) small-grain and (g) large-grain colloidal crystal. (e, h) Colors from the (e) small-grain and (h) large-grain samples linearly mapped onto azimuthal angle ϕ and polar angle θ. (f) Plot of radiant intensity vs θ for each of the RGB channels, obtained by averaging over all values of ϕ. (i) Plot of radiant intensity vs azimuthal angle ϕ derived from the blue channel of (h), ranging $\phi = 0$ to $60°$ averaged over the six fold symmetry regions, at $\theta = 52°$. The solid blue line is the radiant intensity and the shaded region represents standard deviation. The highest peak is from the largest grain, A; the second highest peak is from the second-largest grain, B; and the lowest radiant intensity, denoted by the solid black line, is an

438 estimate of the amount of light from various other small grains, C. The dashed line represents
439 the background illumination of the ping pong ball, measured in a non-colored region. (j)
440 Optical image of the illuminated region, with A, B, and C grain structures identified. (k) SEM
441 image analysis confirms that the largest grain A and the second-largest grain B are relatively
442 orientated at 19.5°.
443
444
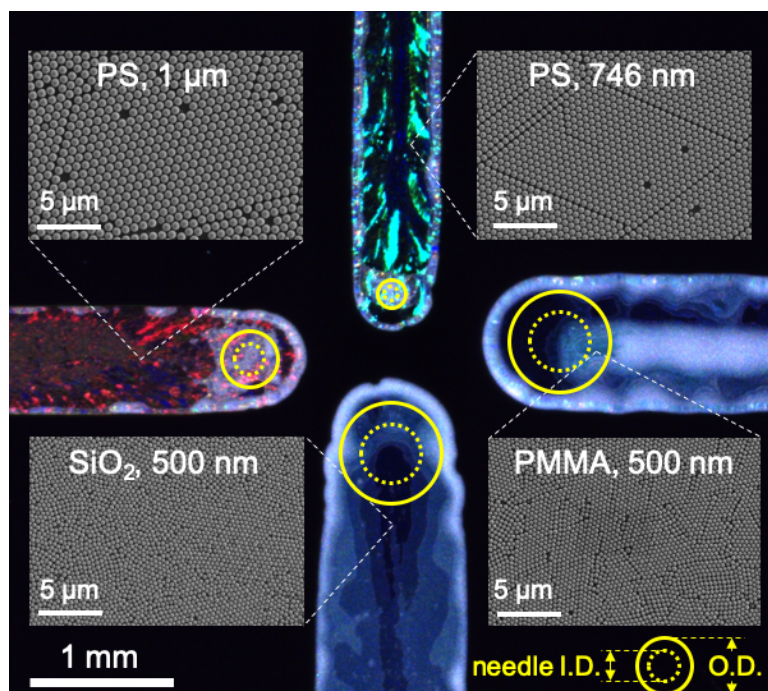
445
446
447 **Figure 5.** Direct-write fabrication of multiple colloidal materials on the same substrate.
448 Clockwise from top: 746 nm polystyrene particles with a needle of OD, ID = 0.2, 0.1 mm;
449 500 nm polymethylmethacrylate (PMMA) particles with a needle of OD, ID = 0.7, 0.4 mm;
450 500 nm silica particles with a needle of OD, ID = 0.7, 0.4 mm; 746 nm polystyrene particles
451 with a needle of OD, ID = 0.4, 0.2 mm. The needle diameters are overlaid on the respective
452 colloidal crystal.
453
454
455

456 **The table of contents entry should be 50−60 words long**, and the first phrase should be
457 bold.
458
460
461 A. T. L. Tan, S. Nagelberg, E. Chang-Davidson, J. Tan, J. K. W. Yang, M. Kolle, A. J. Hart*
462
463 **In-Plane Direct-Write Assembly of Iridescent Colloidal Crystals**
464

465
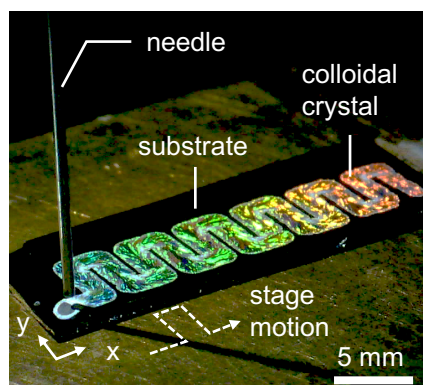
466 Direct-write is presented as a technique for fabricating high quality iridescent colloidal
467 crystals directly from a digital template, without the need for masks or etching. The
468 iridescence is characterized as a means for gaining feedback on grain size and orientation. By
469 stacking multiple print passes, direct-write provides a pathway toward 3-D printing of
470 colloidal crystals.

471

472

Supporting Information

In-Plane Direct-Write Assembly of Iridescent Colloidal Crystals

Alvin T. L. Tan, Sara Nagelberg, Elizabeth Chang-Davidson, Joel Tan, Joel K. W. Yang, Mathias Kolle, A. John Hart*
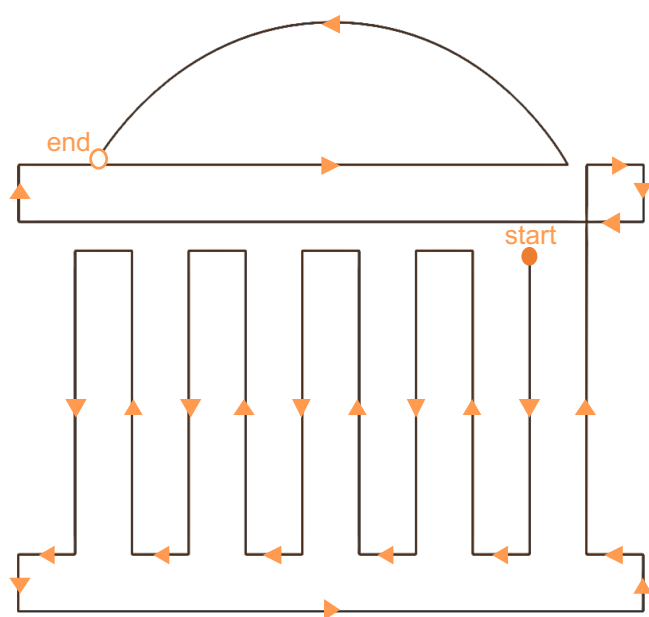
Figure S1. Simple vector graphic (black line) overlaid with the direct-write toolpath (orange arrows) used for fabrication of the colloidal crystal shown in Fig. 3a.
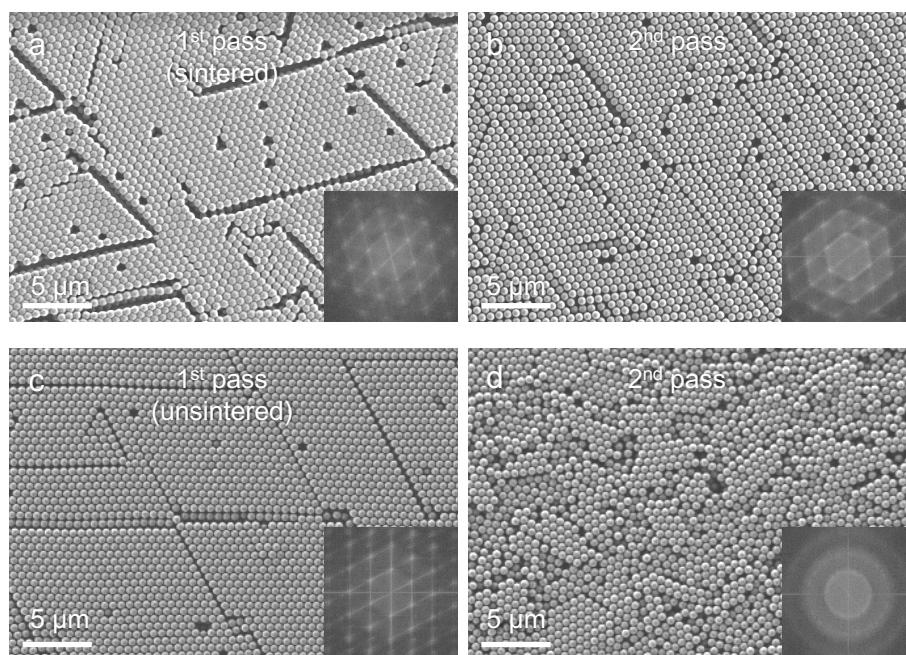
Figure S2. SEM of overlapping passes. (a) Sintered 1st pass. (b) 2nd pass over the sintered 1st pass. (c) Unsintered 1st pass. (c) 2nd pass over the unsintered 1st pass. Insets: 2-D Fast Fourier Transform of the corresponding image. Hexagonal peaks indicate order and the diffuse rings indicate disorder.
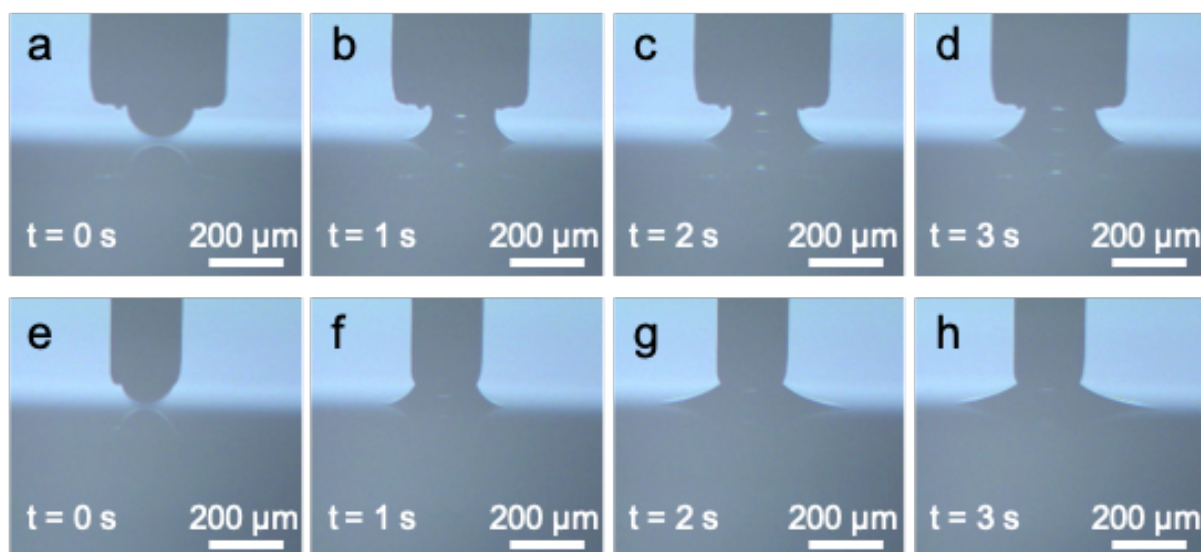
Figure S3. Optical video stills of the meniscus spreading from a 27 gauge needle (a-d) and a 33 gauge needle (e-h). In both cases, the dispense rate is the same (1.57 nL/s). The meniscus spreads quickly from the 33 gauge needle beyond the radius of the needle, thus making the width of the colloidal trace hard to control.

Quantitative Angle Measurements from Ping Pong Ball images.

The ping pong ball as a screen is a clean and simple way of capturing the full color distribution for all viewing angles in just one measurement. From a top view of the ping pong ball it is simple to quantitatively map pixels on the image to precise angles (θ, ϕ). From the center of the ping pong ball (found by manually fitting a circle to the edges using ImageJ)

$$(x, y) = (R \cos(\phi) \sin(\theta), R \sin(\phi) \sin(\theta))$$

35 Unfortunately, an unobstructed top view of the ping pong ball is not always easily captured,
36 particularly when the illumination is at normal incidence. For this reason, we captured the
37 color pattern from a side view of the ping pong ball. We define the viewing direction of the
38 camera as $(\theta_{cam}, \phi_{cam})$ and mapping back from this view to the global coordinates (θ, ϕ)
39 can be done with a coordinate transformation. First, we define a new pair of angles (Δ, γ)
40 measured from the camera to sample axis as shown in Figure S4. Again, measured from the
41 center of the ping pong ball the pixel locations corresponding to these angles are:

$$(x, y) = (R \cos(\gamma) \sin(\Delta), R \sin(\gamma) \sin(\Delta))$$
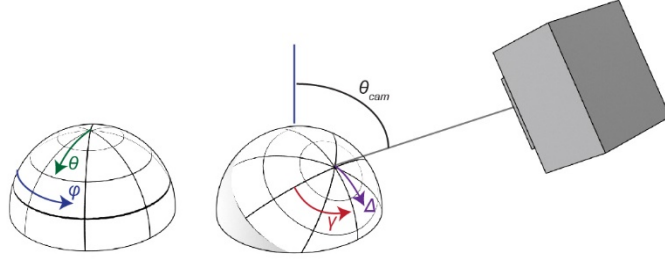
46 **Figure S4. Camera Angle.** Global coordinate system (θ, ϕ) shown as well as the projected
47 system, when imaged at an angle θ_{cam}. Δ is the angle measured from the camera axis, and γ is
48 the azimuthal angle in this rotated coordinate system. By converting from (Δ, γ) coordinates
49 to the global (θ, ϕ) coordinates, we can quantitatively determine the angle to which each
50 color is scattered from photographs taken at an angle.
51 In order to determine (Δ, γ) in terms of (θ, ϕ), consider a point on the surface of the ping
52 pong ball in 3D:

$$\begin{pmatrix} X \\ Y \\ Z \end{pmatrix} = \begin{pmatrix} \cos(\phi)\sin(\theta) \\ \sin(\phi)\sin(\theta) \\ \cos(\theta) \end{pmatrix}$$

56 We then can rotate these coordinates first around the Z-axis by ϕ_{cam} then around the y axis by
57 θ_{cam} to get new coordinates:

$$\begin{pmatrix} X' \\ Y' \\ Z' \end{pmatrix} = \begin{pmatrix} \cos(\theta_{cam}) & 0 & \sin(\theta_{cam}) \\ 0 & 1 & 0 \\ -\sin(\theta_{cam}) & 0 & \cos(\theta_{cam}) \end{pmatrix} \begin{pmatrix} \cos(\phi_{cam}) & -\sin(\phi_{cam}) & 0 \\ \sin(\phi_{cam}) & \cos(\phi_{cam}) & 0 \\ 0 & 0 & 1 \end{pmatrix} \begin{pmatrix} X \\ Y \\ Z \end{pmatrix}$$

61 And then:

$$\beta = \text{atan}\left(\frac{Y'}{X'}\right), \qquad \Delta = \text{acos } Z'$$

64 ## Grain and Colloid Size Estimates
65 From the color distributions, it is possible to gain an estimate of the grain and colloid size in
66 the illuminated area. Each grain will diffract light in a pattern with six-fold symmetry, the
67 angle that each color is scattered to is set by the first order diffraction equation:

$$\sin(\theta) = \frac{\lambda}{d},$$

70 where $d = \frac{\sqrt{3}}{2}D$ is the distance between lattice planes and D is the diameter of the colloids.

71 Figure 4f in the main part of the manuscript shows the radiant intensity as a function of polar

72 angle θ for each of the three color channels, obtained by averaging over all values of ϕ. The

73 peaks can be used to estimate colloid size, by using $\lambda = 490$nm, 550nm, and 650nm as the

74 peak wavelengths for the blue, green, and red channels respectively.[1] This yielded an

75 estimated diameter of 751nm whereas the real colloid size was 747nm.
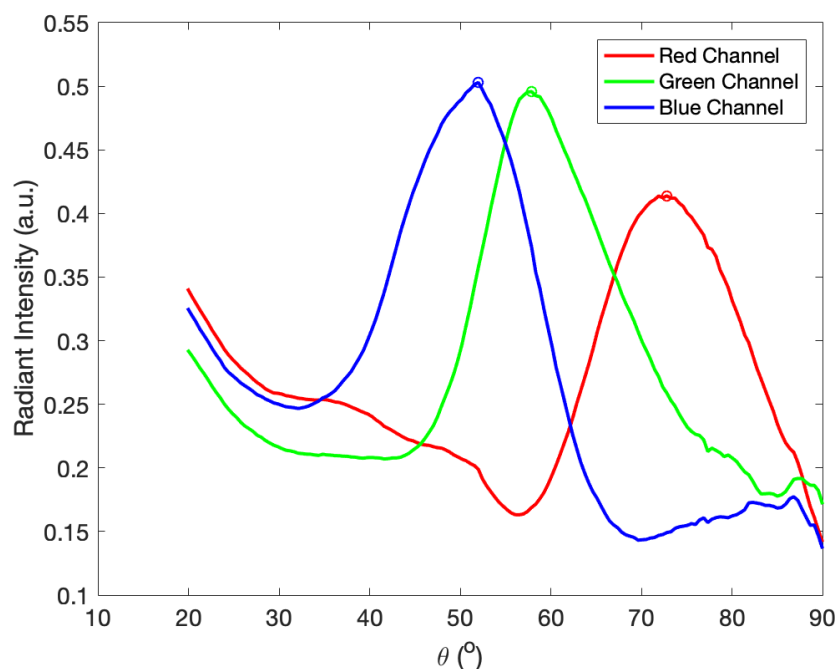
76
77 **Figure S5. Polar angle dependence of the radiant intensity of diffracted light for the**

78 **camera's three color channels.** Radiant intensity measured from ping pong ball photographs

79 for each of the RGB channels. The peak values can be used to determine colloid size.

80
81 More interestingly, the spacing and relative height of diffraction orders in the azimuthal

82 direction gives an estimate of the grain structure. If there are many small grains present, then

83 there will be many individual diffraction patterns with different azimuthal orientations, such

84 that the overall scattered radiant intensity is constant as the azimuthal angle ϕ is varied. If

85 there are only a few grains present, however, distinct peaks are visible in Figure 4g.

86
87 In order to get an estimate of the size of the grains using this technique, we compare the

88 relative radiant intensity of each of the peaks. Because of the six-fold symmetry of the

89 colloidal crystal structure, we only need to look at an azimuthal angle range of 60º of the

90 scattered light; therefore we average each of the 60º sections that is visible in our image of the

91 ping pong ball (Figure S6a and b). Because scattering from the ping pong ball is not perfectly

92 uniform, a white scatterer (Teflon tape) was used to normalize the azimuthal color

93 distributions. The Teflon tape acts a Lambertian scatterer and should not be used to

94 normalize in the polar direction, as its scattering profile does have a θ dependence.

95

96
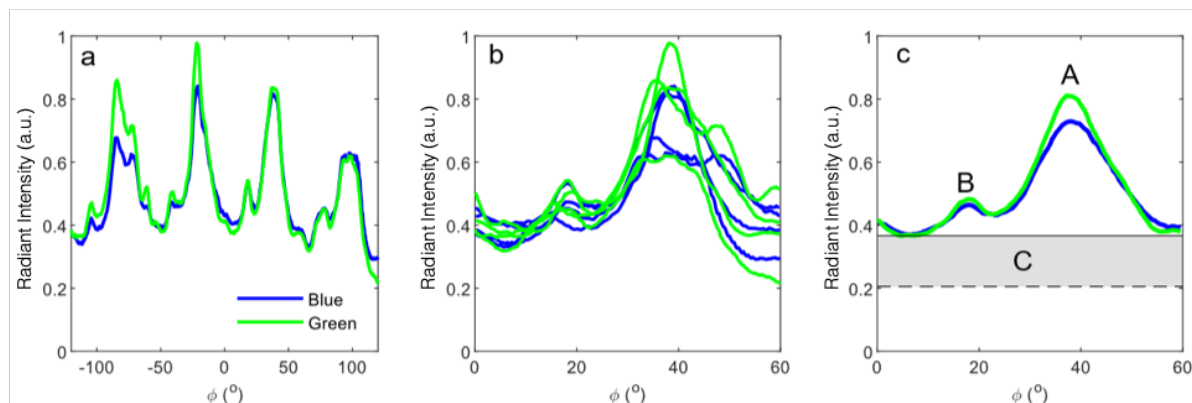
97
98 **Figure S6. Azimuthal Dependence of Diffracted light.** Radiant intensity measured in the
99 color projection at polar angles θ, where peak radiant intensity was observed (see Figure S5).
100 **a)** Radiant intensity of the color projection for the full azimuthal range in the green and blue
101 channel. **b)** The data in (a) folded back over each 60º section. **c)** The average of (b), showing
102 two distinct peaks in radiant intensity corresponding to two large grains. The dashed line
103 represents the background illumination of the ping pong ball, and the solid line represents the
104 minimum corresponding to small randomly oriented grains.

105
106 In the case of the example shown in Figure S6, there are two distinct peaks, as well as a low
107 level continuum of diffraction from small grains. We first subtract off the background that
108 can be associated with the illumination of the ping pong ball (dotted line in Figure S6c). The
109 integral of the area under the curve corresponds to the total light scattered by the printed
110 crystal. The area labeled as C corresponds to light scattered by small randomly oriented
111 smaller grains. A and B correspond to larger grains. The relative height of A and B should
112 correspond to the relative size of these two grains. The uncertainty is estimated from the
113 standard deviation of the different 60º sections.

114
115 From this information, we can estimate that there is a large grain (A) that covers 41% $\pm$ 14%
116 of the illuminated area, a smaller grain (B), rotated about 20º from the first, that covers
117 11% $\pm$ 6% of the illuminated area, and the remaining 48% $\pm$ 17% is covered by small,
118 randomly oriented grains, which corresponds with observations from optical and SEM
119 images, as shown in Figure 4j,k in the main text.

120
121 **References**
122
123 [1]   J. Deglint, F. Kazemzadeh, D. Cho, D. A. Clausi, A. Wong, *Sci. Rep.* **2016**, *6*, DOI
124   10.1038/srep28665.

125